
















Pressure-induced polyamorphic transition in CaAl_2O_4 glass

Itaru Ohira ^{1,*}, Yoshio Kono ^{2,3,†}, Steeve Gréaux ³, James W. E. Drewitt ⁴, Sandro Jahn ⁵, Fumiya Noritake ⁶,
Koji Ohara ^{7,8}, Satoshi Hiroi ^{7,8}, Nozomi M. Kondo ⁹, Rostislav Hrubíak ¹⁰, Yuji Higo ⁸, Noriyoshi Tsujino ⁸,
Sho Kakizawa ⁸, Kiyofumi Nitta ⁸, and Oki Sekizawa ⁸

¹Department of Chemistry, *Gakushuin University*, Toshima-ku, Tokyo 171-8588, Japan

²Department of Physics and Astronomy, *Kwansei Gakuin University*, Sanda 669-1330, Japan

³Geodynamics Research Center, *Ehime University*, Matsuyama 790-0826, Japan

⁴School of Physics, *University of Bristol*, H H Wills Physics Laboratory, Bristol BS8 1TL, United Kingdom

⁵Institute of Geology and Mineralogy, *University of Cologne*, D-50674 Köln, Germany

⁶Graduate Faculty of Interdisciplinary Research, *University of Yamanashi*, Kofu 400-8511, Japan

⁷Faculty of Materials for Energy, *Shimane University*, Matsue 690-8504, Japan

⁸*Japan Synchrotron Radiation Research Institute*, Sayo-gun, Hyogo 679-5198, Japan

⁹Institute for Planetary Materials, *Okayama University*, Misasa 682-0193, Japan

¹⁰High Pressure Collaborative Access Team, X-ray Science Division, *Argonne National Laboratory*, Argonne, Illinois 60439, USA



(Received 30 April 2024; revised 22 May 2024; accepted 2 August 2024; published 28 August 2024)

In situ high-pressure ultrasonic velocity measurements of CaAl_2O_4 glass reveal abrupt irreversible discontinuities in the elastic wave velocities at ~ 8 – 10 GPa. Total structure factor and pair distribution functions measured by synchrotron x-ray diffraction show a rapid change in the intermediate range structure attributed to a rearrangement of calcium ions over this narrow pressure region. Atomistic models obtained from molecular dynamics simulations reveal that this intermediate range structure is explained by a transition of Ca–O void radius distribution from a bimodal distribution with peaks at ~ 2.1 and ~ 2.4 Å to a single distribution centered at ~ 2.1 Å. These abrupt structural changes involving the rapid increase in elastic wave velocity are markedly different to the continuous transformations observed in conventional network-forming glasses, such as SiO_2 .

DOI: [10.1103/PhysRevB.110.054115](https://doi.org/10.1103/PhysRevB.110.054115)

I. INTRODUCTION

Pressure-induced changes in the structure and physical properties of oxide glasses are of great interest in condensed matter physics and materials science. There have been extensive studies on the high-pressure behavior of network-forming oxide glasses such as SiO_2 , GeO_2 , TiO_2 , TeO_2 , and B_2O_3 glasses (e.g., Refs. [1–20]). Network-forming oxide glasses are known to exhibit anomalous elasticity behavior at high-pressure conditions. For example, SiO_2 glass, a prototypical network glass former, exhibits an anomalous elasticity minimum under compression at ~ 2 – 3 GPa [1–3], which likely arises from the onset of penetration of the Si atoms from the second shell into first shell [4]. This local tetrahedral symmetry breaking is followed by a further collapse in the intermediate range structural ordering (e.g., Refs. [5–7]). Above ~ 10 GPa, the elastic wave velocity gradually increases, accompanied by a continuous change in nearest-neighbor Si–O coordination number (CN) from 4 to 6 [5–10], and exhibits irreversibility in the elastic properties and optical spectra [1,3,11–13].

In recent years, there has been increasing emphasis on the fabrication and characterization of nonconventional

network glass formers such as CaO – Al_2O_3 [21–25], BaO – Al_2O_3 [22,26], BaO – TiO_2 [27], La_2O_3 – Ga_2O_3 [28], and La_2O_3 – Nb_2O_3 [29]. Compared with conventional network glasses, these glasses generally exhibit high packing density [30] and enhanced optical and mechanical functional properties, including a wide infrared transmission window [31], high elastic modulus and hardness [32,33], high crack resistance [34], and high refractive index [35,36]. While the influence of composition on the structures and properties of these types of oxide glasses has been relatively well studied, the effect of pressure has not been extensively explored. A fundamental question is whether the high-pressure behavior of these densely packed oxide glasses is like that of common network-forming oxide glasses.

In this paper, we have measured the high-pressure elastic wave velocity and structure of the nonconventional aluminate glass CaAl_2O_4 . In addition to the velocity measurements, we have conducted synchrotron x-ray diffraction measurements and molecular dynamics (MD) simulations, which provided a structural view for the elastic behavior of the glass sample. From these combined approaches, we reveal abrupt pressure-induced structure changes in CaAl_2O_4 glass.

II. METHODS

The CaAl_2O_4 glass samples were synthesized using an aerodynamic levitation furnace at Tohoku University [37].

*Contact author: itaru.ohira@gakushuin.ac.jp

†Contact author: yoshiokono@kwansei.ac.jp

In addition to the CaAl_2O_4 glass samples, a disk of SiO_2 glass was prepared from a commercial SiO_2 glass rod. Details of sample preparation are shown in the Supplemental Material [38].

A. *In situ* high-pressure ultrasonic measurements

The elastic wave velocities of CaAl_2O_4 glass at high pressures were measured by *in situ* x-ray and ultrasonic measurements in a Kawai-type 1500 ton multianvil press apparatus (SPEED-1500) at the beamline BL04B1 in SPring-8 [39,40]. The cell assembly is mainly composed of a Mg-CoO octahedron pressure medium and an inner MgO sleeve. This assembly is based on a design reported in our previous work [41], simplified for room-temperature measurements. The glass samples were shaped into a cylindrical shape using diamond mats (~ 2 mm in diameter and ~ 1 mm in length) and placed at the center of a MgO sleeve. Both sides of the samples were polished using $0.5 \mu\text{m}$ diamond paste. We placed an Al_2O_3 buffer rod for transmitting elastic waves from the WC anvil to the sample, and a backing material (NaCl with 10 wt.% gold) was placed at the back side of the sample. A gold foil ($2 \mu\text{m}$ thickness) was inserted between each interface (buffer rod/sample and sample/backing material) to enhance mechanical coupling for elastic wave propagation and to mark sample interfaces for sample length measurement.

X-ray radiography images were obtained using a charge-coupled device camera with a pixel size of $1.31 \mu\text{m}$. Sample lengths were determined by analyzing the distance between the two gold foils at the ends of the sample. For pressure determination, energy-dispersive x-ray diffraction (EDXD) measurements were made of the backing material at a fixed diffraction angle of 6.0052° (Exp. 1) or 6.0040° (Exp. 2). The unit-cell volumes of gold calculated from the three reflections (111, 200, and 220) were used to determine pressure by reference to the equation of state of gold reported in Ref. [42]. Ultrasonic measurements were carried out at each pressure condition using the pulse–echo–overlap method. The acoustic echo measurements were performed at the frequency of 60 MHz for longitudinal waves and 40 MHz for transverse waves. The two-way travel time was analyzed by using an analysis program [43].

The errors of sample length analysis were defined as the standard deviation of the distance between the buffer rod/sample and sample/backing reflector interfaces [43], which was up to ± 4.4 pixel ($\pm 6 \mu\text{m}$, 0.6%). The errors of travel time analyses were up to 0.6% (longitudinal wave) and 0.2% (transverse wave), respectively. The overall uncertainties of longitudinal and transverse wave velocities (v_L and v_T , respectively) are up to 0.6%. The numerical data of v_L and v_T with their uncertainties are shown in Tables S1–S3 in the Supplemental Material [38]. Poisson’s ratio σ is calculated directly from the determined velocities by the equation:

$$\sigma = \frac{v_L^2 - 2v_T^2}{2(v_L^2 - v_T^2)}. \quad (1)$$

B. *In situ* high-pressure multiangle EDXD measurement

The high-pressure structure factors $S(Q)$ of CaAl_2O_4 glass were measured using *in situ* multiangle EDXD measurements

in a Paris-Edinburgh press at the beamline 16-BM-B of the Advanced Photon Source (APS). Details of the high-pressure experimental setup at beamline 16-BM-B and the analytical procedures employed have been previously reported [44–46]. We used a cupped-Drickamer-toroidal (CDT) cell [46]. For room-temperature measurements, a TiB_2 heater and a LiF capsule used in Ref. [46] were replaced with a BN capsule. A piece of gold was used as a pressure marker [42], which was placed at the edge of the glass sample to avoid contamination of x-ray diffraction peaks of gold into that of the glass sample.

In multiangle EDXD measurements, we collected a series of EDXD patterns of the CaAl_2O_4 glass sample at 2θ angles of 3.1, 4.1, 5.1, 7.1, 9.1, 12.1, 15.1, 22.1, 26.1, and 35.1° at each pressure point. The $S(Q)$ was determined from the collected EDXD patterns using the aEDXD program developed by Park and Hrubyak at the 16-BM-B beamline [44]. The pair distribution function $g(r)$ was calculated by Fourier transform of $S(Q)$ using the density for CaAl_2O_4 glass determined by polarizable ion model MD (PIM-MD) simulations [24]. The peak positions in $g(r)$ were determined by Gaussian fitting.

C. $S(Q)$ measurement at ambient conditions

$S(Q)$ measurements of the unpressurized and densified CaAl_2O_4 glasses at ambient conditions were conducted at the BL37XU beamline in SPring-8 [47]. We used a monochromatic beam at a photon energy of 37.5 keV, and x-ray diffraction measurements were carried out by scanning 2θ angles from 1 to 62° , which corresponds to a Q range of 0.3–19.5 \AA^{-1} . The data was analyzed using the method described in Ref. [47]. We used densities of the unpressurized CaAl_2O_4 glass ($2.90 \pm 0.02 \text{ g/cm}^3$) and the densified CaAl_2O_4 glasses recovered from the multiangle EDXD measurement to 9.8 GPa ($3.06 \pm 0.04 \text{ g/cm}^3$) and the ultrasonic measurement to 24.2 GPa ($3.18 \pm 0.02 \text{ g/cm}^3$) measured by Archimedes’ method.

D. MD simulations

In this paper, we used PIM-MD [24] and the PMMCS potential (PMMCS-MD, Ref. [48]). For the PIM-MD simulations developed in Refs. [49,50], the technical details and results for CaAl_2O_4 liquids and quenched glasses at high pressures were reported in Ref. [24]. Here, we extended the previous study by developing structural models of CaAl_2O_4 glasses under cold compression and cold decompression. As starting structure, we used the glass that was obtained after quenching a melt at a constant pressure of 0 GPa from 2500 to 300 K with a rate of 10^{12} K/s [24]. The simulation cell contained a total of 1512 atoms for CaAl_2O_4 , i.e., 864 ions of O, 432 ions of Al, and 216 ions of Ca. Compressed glasses were obtained by stepwise increase of pressure by 5 GPa and equilibration runs at constant pressure and 300 K (NPT ensemble) for 50 ps until 30 GPa were reached. At each pressure, structural properties were derived from additional simulations at constant volume (NVT ensemble) for 20 ps. Note that the first pressure point during compression was set to 6 GPa instead of 5 GPa for no specific reason and without any consequence for the results presented here. The final structure after equilibration at 30 GPa was used as the

starting structure for the decompression of the glass, which was performed by reducing the pressure in steps of 5 GPa and performing the same simulations as during compression. The initial and final glasses before compression and after decompression, both at 0 GPa and 300 K, had densities of 2.84 and 3.13 g/cm³, respectively.

The annealing simulations for the densified structural model after decompression ($\rho = 3.13$ g/cm³) were also performed at 0 GPa by PIM-MD. In the simulations, the temperature of the simulation cells was increased to target temperature in 1 fs and annealed for 220 ps. After 220 ps, the temperature was set to 300 K again and the simulations continued by another 10 ps to reach a total simulation time of 230 ps.

In the PMMCS-MD simulations, MXDORTO code [51] was used. Here, 1429 atoms of Ca, 2858 atoms of Al, and 5716 atoms of O were placed in the cell, and all the atoms were moved by applying the velocity Verlet algorithm [52,53] at a time interval of 1.0 fs. Long-range Coulombic interactions were treated by using Ewald summations. The structural relaxation from a randomly coordinated system was performed at 3000 K with NVT ensembles for 5.0 ns, followed by quenching to 300 K at the rate of 1×10^{12} Ks⁻¹, at constant density of 3.06 and 3.18 g/cm³, the same as the density values of the densified glasses recovered from the two *in situ* experiments. Then the structure was relaxed also at 300 K with NVT ensembles for 2.0 ns, and the trajectories of atoms were obtained under NVT ensembles at 300 K for 1.0 ns by an interval of 100 fs.

III. RESULTS AND DISCUSSIONS

The longitudinal (v_L) and transverse (v_T) wave velocities of CaAl₂O₄ glass, as determined by *in situ* high-pressure ultrasonic measurements, are shown in Fig. 1 up to 24.1 GPa, compared with the corresponding results for SiO₂ glass from this paper and previous work [2]. Below 8 GPa, v_L and v_T decrease slightly and continuously with increasing pressure, followed by an abrupt increase in both values over the narrow range of 8–10 GPa (Fig. 1). Above ~ 10 GPa, v_L and v_T continue to increase gradually and continuously with increasing pressure, which is like SiO₂ glass. On decompression from 16 GPa, v_L and v_T exhibit an irreversible change (Fig. 1), with v_L and v_T 12 and 13% higher at 5.3 GPa during decompression than at 5.5 GPa during compression, respectively. The observed discontinuity in wave velocity is accompanied by an abrupt 5–6% reduction in sample length (L) during compression over the narrow pressure range of 8–10 GPa (Fig. S1(a) in the Supplemental Material [38]). Over the entire pressure range, L/L_0 (L_0 is the sample length before compression) reduces by $\sim 17\%$, recovering to only 86% of its original length at 1.7 GPa during decompression. In contrast with the abrupt changes observed in v_L , v_T , and L , there is no marked change in the Poisson ratio (σ) of CaAl₂O₄ glass up to 24 GPa, which exhibits a reversible change during the compression and decompression cycle (Fig. S1(b) in the Supplemental Material [38]).

The high-pressure behavior of v_L , v_T , and L for CaAl₂O₄ glass up to ~ 10 GPa is markedly different from that of SiO₂ glass. Below ~ 3 –5 GPa, v_L and v_T for SiO₂ glass decrease

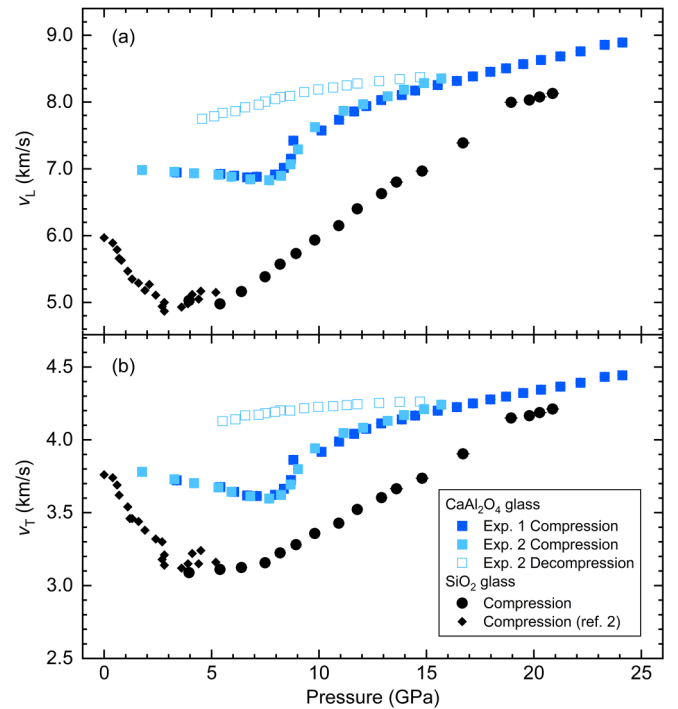


FIG. 1. (a) Longitudinal (v_L) and (b) transverse (v_T) wave velocities of CaAl₂O₄ glass (blue) and SiO₂ glass (black) up to 24.1 GPa. Solid blue and light blue squares represent the data measured under compression in two experiments (Exp. 1 and 2), and open light blue squares represent the data obtained under the decompression process in Exp. 2. Solid black circles and diamonds represent v_L and v_T of SiO₂ glass measured in this paper and reported in a previous ultrasonic measurement [2], respectively. The errors of pressure, v_L , and v_T are within the sizes of symbols. The numerical data are shown in Tables S1–S3 in the Supplemental Material [38].

rapidly with increasing pressure, before switching to a gradual increase with pressure at higher pressure conditions (Fig. 1). There is no sharp discontinuity in the velocity curves of SiO₂ glass at high pressures. In addition, the sample length of the SiO₂ glass shows continuous shortening across the entire range of pressure (Fig. S1(a) in the Supplemental Material [38]). These data indicate a significant difference in the high-pressure behavior of densely packed CaAl₂O₄ glass compared with the typical network forming SiO₂ glass. Specifically, the abrupt discontinuity observed in v_L , v_T , and L over the narrow range 8–10 GPa for CaAl₂O₄ glass implies the possible existence of a polyamorphic transition.

To understand the high-pressure structure, we performed *in situ* multiangle EDXD measurements on CaAl₂O₄ glass at pressures up to 9.8 GPa at the beamline 16-BM-B of the APS (Figs. 2 and S2 in the Supplemental Material [38]). On initial compression, the height of the first sharp diffraction peak (FSDP) of the total structure factor $S(Q)$ increases slightly and shifts toward higher scattering vectors Q . Between 7.0 and 9.1 GPa, the FSDP experiences a particularly rapid development in height and position, accompanied by the rapid appearance of a new subsidiary peak at $\sim 2.8 \text{ \AA}^{-1}$ [Fig. 2(a)]. The rapid development of this subsidiary peak can be attributed to an increase in topological ordering due to an abrupt transition to a more densely

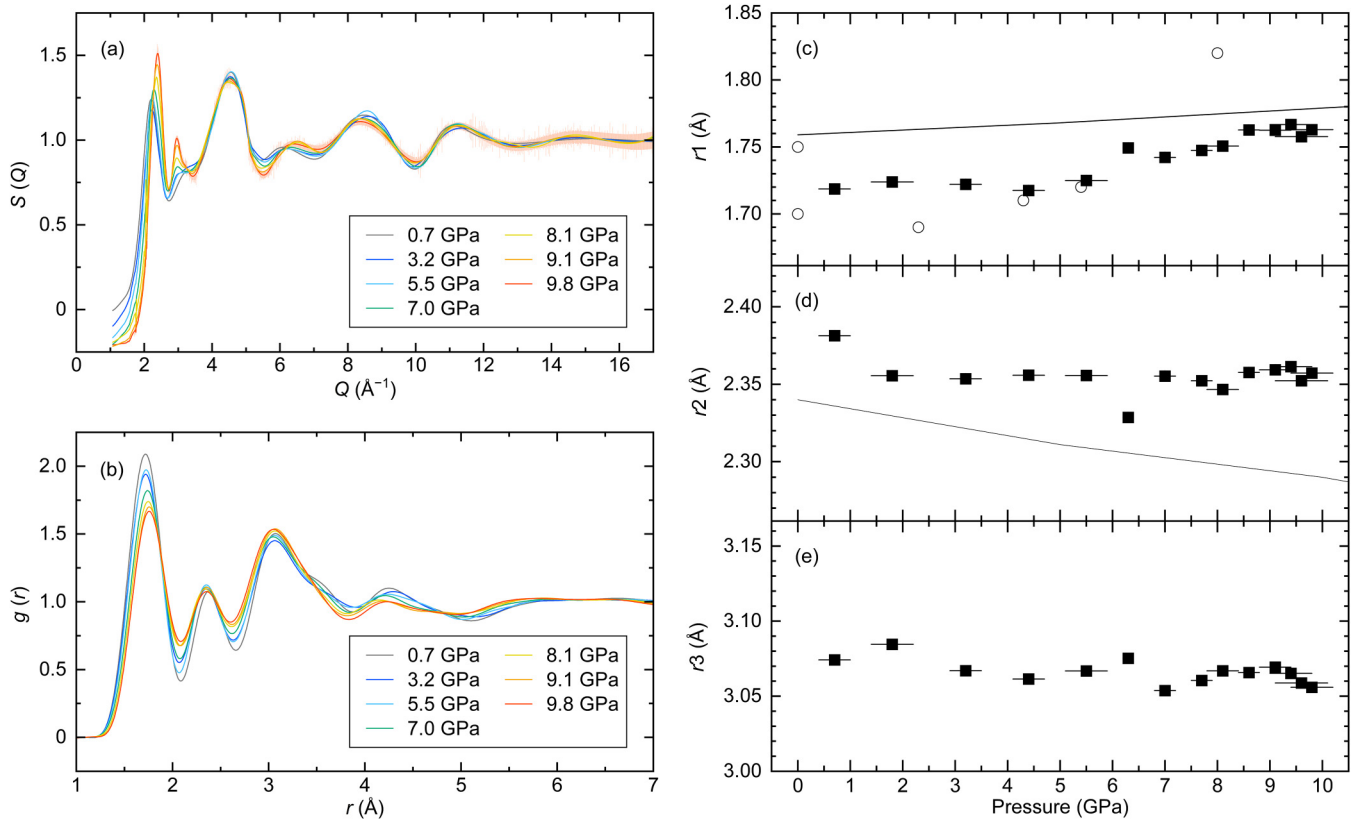


FIG. 2. (a) Total structure factor $S(Q)$ for CaAl_2O_4 glass as measured by *in situ* multiangle energy-dispersive x-ray diffraction (EDXD) at 0.7, 7.0, 8.1, 9.1, and 9.8 GPa. A typical size of the error is indicated by the pink vertical bars for the $S(Q)$ data at 9.8 GPa. The full range of measurements with error bars are shown in Fig. S2(a) in the Supplemental Material [38]. (b) $g(r)$ of CaAl_2O_4 glass as determined from the Fourier transform of the corresponding $S(Q)$ functions in (a). The full range of $g(r)$ data obtained is shown in Fig. S2(b) in the Supplemental Material [38]. (c)–(e) The first (r_1), second (r_2), and third peak (r_3) positions in the $g(r)$ of CaAl_2O_4 glass at high pressures. Square symbols indicate the results obtained in this paper. The open circles in (c) indicate the Al–O bond length obtained by previous *in situ* x-ray diffraction (XRD) measurements [24]. The lines in (c) and (d) show the pressure dependence of Al–O and Ca–O bond lengths, respectively, as determined from polarizable ion model molecular dynamics (PIM-MD) simulations [24].

packed structure [54]. In real space, the total pair distribution function $g(r)$, as determined from the Fourier transform of $S(Q)$, shows no abrupt change in the first, second, and third peak positions (r_1 , r_2 , and r_3 , respectively) within the experimental pressure range up to 9.8 GPa [Fig. 2(b)]. The position of the r_1 (Al–O) peak remains constant <5 GPa, before gradually increasing at higher pressures [Fig. 2(c)], considered due to a gradual increase of the Al–O CN [24]. The positions of the r_2 and r_3 peaks attributed to Ca–O and Al–Ca/Al distances, respectively, do not undergo any substantial change at high pressures [Figs. 2(d) and 2(e)]. However, a shoulder on the high r side of the r_3 peak located at ~ 3.6 \AA at low pressure vanishes beyond 8.1 GPa [Fig. 2(b)].

The major changes in the FSDP, the appearance of the subsidiary peak at ~ 3 \AA^{-1} in $S(Q)$ and the disappearance of the shoulder at ~ 3.6 \AA in $g(r)$, occur over the same pressure region (~ 8 – 10 GPa) as the abrupt changes observed in the elastic wave velocities and sample length. This indicates that the intermediate range structure is key to understanding the high-pressure discontinuities observed in CaAl_2O_4 glass. Previous nuclear magnetic resonance measurements of high-pressure cycled CaAl_2O_4 and $13\text{CaO}\cdot 7\text{Al}_2\text{O}_3$ glasses

revealed a modest but irreversible increase in the Al–O CN at 8–12 GPa [55,56], attributed to an irreversible structural change, consistent with our observation of irreversible change in elastic wave velocity and sample length. In addition, the CaAl_2O_4 glass sample recovered from 9.8 GPa after the high-pressure EDXD measurement exhibits permanent densification, with a 6% increase in density [$3.06(3)\text{g/cm}^3$] compared with the original glass [$2.90(2)\text{g/cm}^3$].

The structures of the densified CaAl_2O_4 glasses recovered from the high-pressure EDXD measurement up to 9.8 GPa [$3.06(3)\text{g/cm}^3$] and the high-pressure ultrasonic measurement up to 24.1 GPa [$3.18(3)\text{g/cm}^3$], together with the original unpressurized CaAl_2O_4 glass sample, were investigated using high-energy x-ray diffraction at the BL37XU beamline in SPring-8. The high-pressure features observed in the *in situ* measurements at >7.0 GPa (Fig. 2), namely, the enhanced FSDP and subsidiary peak at ~ 3 \AA^{-1} in $S(Q)$ and the disappearance of the peak shoulder at ~ 3.6 \AA in $g(r)$, are preserved in the two pressure-recovered glasses (Figs. S3 and S4 in the Supplemental Material [38]). These differences between the pressurized and unpressurized glasses are consistent with the previous observation using high-energy x-ray diffraction measurement [57].

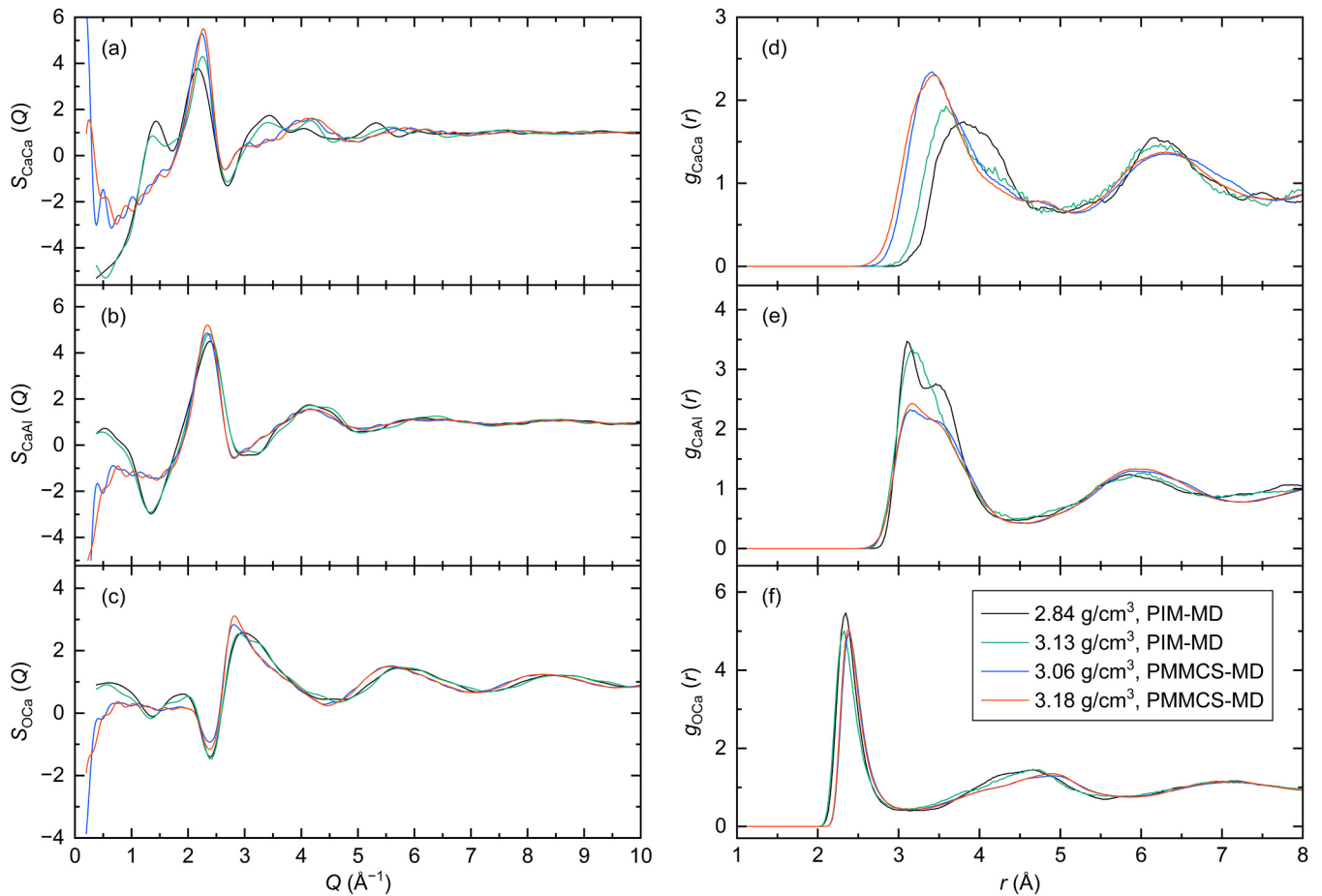


FIG. 3. Partial structure factors $S_{ij}(Q)$ and partial pair distribution functions $g_{ij}(r)$, for calcium-related correlations of the CaAl_2O_4 glasses calculated by molecular dynamics (MD) simulations: (a) $S_{\text{CaCa}}(Q)$, (b) $S_{\text{CaAl}}(Q)$, (c) $S_{\text{OCa}}(Q)$, (d) $g_{\text{CaCa}}(r)$, (e) $g_{\text{CaAl}}(r)$, and (f) $g_{\text{OCa}}(r)$. The MD simulations were carried out for the densities of 2.84 g/cm^3 (black) corresponding to that of the unpressurized glass and 3.06 g/cm^3 (blue), 3.13 g/cm^3 (green), 3.18 g/cm^3 (red) corresponding to those of pressurized glasses. The full set of $S_{ij}(Q)$ and $g_{ij}(r)$ including the other correlations is shown in Fig. S5 in the Supplemental Material [38].

We constructed structural models which reproduce the experimentally observed $S(Q)$ by PIM-MD (Figs. 3 and S3 and S5 in the Supplemental Material [38]). The structural models indicate that the abrupt change observed in the FSDP coincides with the development of strong peak in the Ca–Ca partial structure factor during compression [Fig. 3(a)]. In terms of coincidence of peak positions, the growth of the subsidiary peak at $\sim 2.8 \text{ \AA}^{-1}$ in the experimental $S(Q)$ likely corresponds to the O–Ca correlation, although this change is not clearly observed between the partial structure factors of the unpressurized and densified structural models [Fig. 3(c)]. In the structural models by PMMCS-MD using the cell-size 6.6 times larger than PIM-MD [Fig. 3(c)], however, the $S_{\text{OCa}}(Q)$ is developed at $\sim 2.8 \text{ \AA}^{-1}$, which coincides with the $S(Q)$ of the densified samples.

In real space, the disappearance of the shoulder on the peak at $\sim 3.6 \text{ \AA}$ in $g(r)$ can be attributed to reduced contribution at this distance from the Ca–Ca and Ca–Al partial pair distribution functions. These high-pressure features are observed more clearly in the comparison between the unpressurized structural model obtained by PIM-MD and the densified structural models obtained by PMMCS-MD [Figs. 3(d) and 3(e)]. The PIM-MD simulations exhibit a development of new peak

at 2.6 \AA in $g_{\text{AlAl}}(r)$ (Fig. S5(d) in the Supplemental Material [38]), which may be attributed to an increase in edge-sharing AlO_x polyhedron. However, it is difficult to identify the new peak at 2.6 \AA in the $g(r)$ experimentally obtained from the *in situ* EDXD (Figs. 2 and S2 in the Supplemental Material [38]), possibly due to multiple components in the experimental $g(r)$ determined by the x-ray diffraction measurements and insufficient resolution of the $g(r)$ by the limited experimental Q range, although the ambient-pressure $g(r)$ results show slight increase in the intensity at $\sim 2.6 \text{ \AA}$ in the densified CaAl_2O_4 glasses (Fig. S4 in the Supplemental Material [38]). In addition, the $g_{\text{AlAl}}(r)$ of the structural models obtained by PMMCS-MD does not show a new peak at this distance (Fig. S5(d) in the Supplemental Material [38]). Therefore, in the real samples, the irreversible change of Al–Al correlation (i.e., increase in edge-sharing AlO_x) seems not to be as pronounced as predicted by PIM-MD.

To understand the three-dimensional picture of the changes observed in the experimentally and computationally determined $S(Q)$ and $g(r)$, we conducted void radius analysis for the structural models of the unpressurized and densified CaAl_2O_4 glasses. In this analysis, the structure models obtained by the PIM-MD and PMMCS-MD simulations are

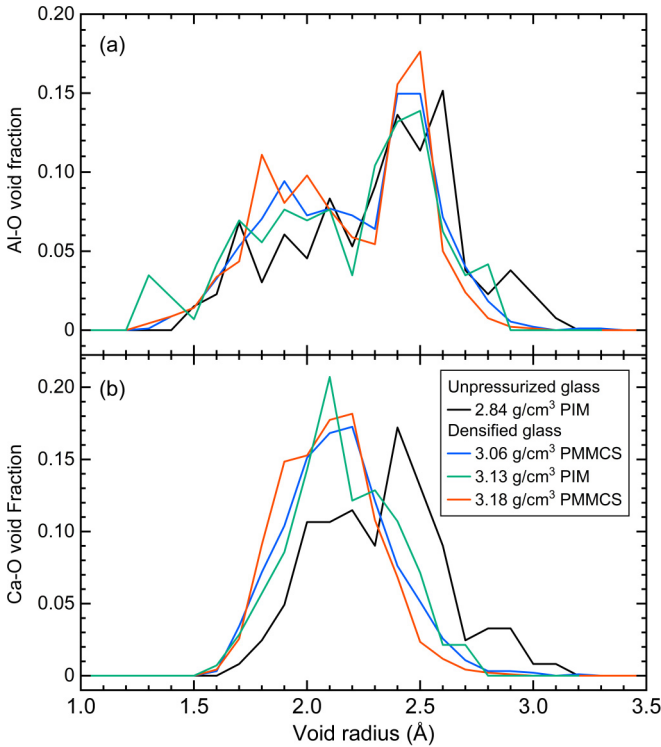


FIG. 4. Void radius distributions formed from (a) aluminum and oxygen atoms (Al–O void radius) and (b) calcium and oxygen atoms (Ca–O void radius) in the unpressurized and densified CaAl_2O_4 glasses, as determined from the structural models computed by molecular dynamics (MD).

divided into a set of tetrahedra by the Delaunay tetrahedralization for Al and O atoms without Ca atoms and Ca and O atoms without Al atoms to investigate distributions of Al–O and Ca–O polyhedron distributions, respectively. A circumscribed sphere of the tetrahedron is defined as a void [58]. If multiple voids overlap, only the largest one is employed in the analysis.

We find no clear distinction between the void structures formed by Al and O atoms in the unpressurized and densified glasses, except for the slight increase in the fraction of small Al–O voids ($\sim 1.7\text{--}2.1$ Å) [Fig. 4(a)]. However, there is a distinct difference in the void structures formed by Ca and O atoms in the unpressurized and densified glass structures [Fig. 4(b)]. The unpressurized CaAl_2O_4 glass exhibits a bimodal distribution in the Ca–O void radius with peaks at ~ 2.1 and ~ 2.4 Å, which is like the distribution of the Al–O void radius. In contrast, for the densified CaAl_2O_4 glasses, we find a single distribution of Ca–O void structures centered at ~ 2.1 Å, while the Al–O void radius structure remains bimodal.

To confirm high-pressure behavior of the void structure, we conducted PIM-MD simulations and void radius analysis for the simulated structural models under compression to 30 GPa and their subsequent decompression. The irreversible changes in the structural correlations involving Ca are also confirmed in this cycle (Figs. S6 and S7 in the Supplemental Material [38]). The void radius formed by Al and O atoms decreases with increasing pressure, and it changes almost reversibly under compression and decompression (Fig. S8 in

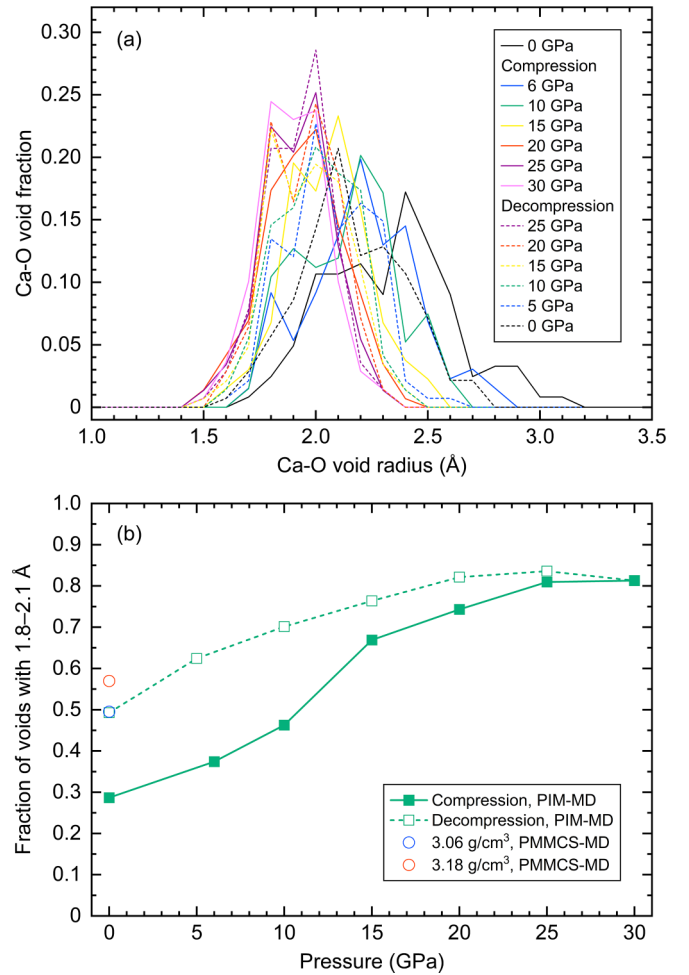


FIG. 5. (a) Change of distributions of Ca–O void radius under compression and decompression processes for the structural models calculated by the polarizable ion model molecular dynamics (PIM-MD) simulations. (b) Pressure dependence of the fraction of Ca–O void structure with $1.8\text{--}2.1$ Å in diameter.

the Supplemental Material [38]). In contrast, the Ca–O void structure also shrinks with increasing pressure but does not recover after decompression (Fig. 5). The proportion of the void radius structure at $1.8\text{--}2.1$ Å abruptly increases from 6 to 15 GPa, and it remains during decompression to 0 GPa (Fig. 5).

The densified CaAl_2O_4 glass decompressed from 30 to 0 GPa has density $\rho = 3.13$ g/cm³, which is $\sim 10\%$ larger than that of unpressurized glass ($\rho = 2.84$ g/cm³). To check back-transformation of the densified glass to the original unpressurized glass, we conducted an annealing test of the densified CaAl_2O_4 glass structure at 0 GPa and 500–1700 K by the PIM-MD simulations (Fig. S9 in the Supplemental Material [38]). The result shows recovery of the volume from the densified glass to the original unpressurized glass with increasing temperature and annealing at >1500 K yields almost same volume structure as the original glass. The result indicates back-transformation of the dense high-pressure structure to the original low-pressure structure.

Our PIM-MD simulations to 30 GPa reveal that an abrupt, irreversible change in the Ca–O void structure drives a

polyamorphic transition in pressurized CaAl_2O_4 glass, resulting in the observed irreversible changes in elastic wave velocities and intermediate-range order. It is important to note that pressure-induced structural change in CaAl_2O_4 glass is distinct from that of SiO_2 glass, a prototypical network-forming oxide glass. At low pressures, structural change of SiO_2 glass occurs by breaking of tetrahedral symmetry in the Si–O network structure. Although this change corresponds to the disappearance of voids formed from Si atoms with a radius of $>3.6 \text{ \AA}$ [4], it does not cause an abrupt increase in wave velocity. At pressures higher than $\sim 10 \text{ GPa}$, the intermediate range structure of SiO_2 glass collapses with the gradual formation of a higher coordinated network of Si–O polyhedral continuing up to $\sim 40 \text{ GPa}$ [5], consistent with the gradual increase observed in the elastic wave velocity [1,3]. In contrast, CaAl_2O_4 glass experiences a markedly different pressure-induced structural change, with an abrupt and irreversible increase in elastic wave velocity over the narrow pressure range of 8–10 GPa. This polyamorphic change is controlled by the transition of the Ca–O void structure from a bimodal to a single distribution, rather than a change in network-former (Al)-related structure.

IV. CONCLUSIONS

To understand the pressure-induced structure changes in CaAl_2O_4 glass, an example of a nonconventional network-forming oxide glass, we conducted *in situ* high-pressure velocity measurements, synchrotron XRD measurements, and MD simulations. The experimentally determined velocity-pressure curves of CaAl_2O_4 glass exhibit abrupt and irreversible increases in v_L and v_T at $\sim 8\text{--}10 \text{ GPa}$, which is correlated with a change in intermediate-range structure involving rearrangement of Ca ions observed in the $S(Q)$ and $g(r)$. Further

analyses for the void structures in the unpressurized and densified glasses reveal that this change in intermediate-range structure arises from the transition of Ca–O void radius distribution from a bimodal distribution to a single and shorter distribution. Our results demonstrate that the drastic change in the Ca–O void structure occurs at $\sim 8\text{--}10 \text{ GPa}$, which causes the polyamorphic transition of CaAl_2O_4 glass, marked by the abrupt and irreversible velocity increases, and likely contributes to the preservation of high-coordinated AlO_x units ($x = 5, 6$) in the densified glass recovered from $>10 \text{ GPa}$ [55,56].

ACKNOWLEDGMENTS

We thank Tomoki Nakamura (Tohoku University) for providing an opportunity to use a containerless laser-heating apparatus. We also thank Hikari Mita (Tohoku University) for help in the syntheses of glass samples. This paper is supported by JSPS KAKENHI (Grants No. JP20K22369, No. JP23K13193, No. JP19KK0093, No. JP20H00201, No. JP23KK0065, and No. JP19H02002), JSPS Bilateral Program (Grant No. JPJSBP120209926), and the Joint Usage/Research Center PRIUS, Ehime University, Japan. The experiments were conducted at the beamlines BL04B1 (JASRI Proposals No. 2020A0069, No. 2020A1712, and No. 2022B1171) and BL37XU (JASRI Proposals No. 2021A1068 and No. 2022A1126) in SPring-8 and at the beamline 16-BM-B in APS. Portions of this work were performed at HPCAT (Sector 16), APS, Argonne National Laboratory. HPCAT operations are supported by the U.S. Department of Energy (DOE) NNSA's Office of Experimental Sciences. The APS is a DOE Office of Science User Facility operated for the DOE Office of Science by Argonne National Laboratory under Contract No. DE-AC02-06CH11357.

-
- [1] C.-s. Zha, R. J. Hemley, H.-k. Mao, T. S. Duffy, and C. Meade, *Phys. Rev. B* **50**, 13105 (1994).
- [2] A. Yokoyama, M. Matsui, Y. Higo, Y. Kono, T. Irifune, and K.-i. Funakoshi, *J. Appl. Phys.* **107**, 123530 (2010).
- [3] C. Weigel, M. Mebarki, S. Clément, R. Vacher, M. Foret, and B. Rufflé, *Phys. Rev. B* **100**, 094102 (2019).
- [4] Y. Kono, K. Ohara, N. M. Kondo, H. Yamada, S. Hiroi, F. Noritake, K. Nitta, O. Sekizawa, Y. Higo, Y. Tange *et al.*, *Nat. Commun.* **13**, 2292 (2022).
- [5] A. Zeidler, K. Wezka, R. F. Rowlands, D. A. J. Whittaker, P. S. Salmon, A. Polidori, J. W. E. Drewitt, S. Klotz, H. E. Fischer, M. C. Wilding *et al.*, *Phys. Rev. Lett.* **113**, 135501 (2014).
- [6] C. J. Benmore, E. Soignard, S. A. Amin, M. Guthrie, S. D. Shastri, P. L. Lee, and J. L. Yarger, *Phys. Rev. B* **81**, 054105 (2010).
- [7] T. Sato and N. Funamori, *Phys. Rev. B* **82**, 184102 (2010).
- [8] Y. Kono, Y. Shu, C. Kenney-Benson, Y. Wang, and G. Shen, *Phys. Rev. Lett.* **125**, 205701 (2020).
- [9] C. Prescher, V. B. Prakapenka, J. Stefanski, S. Jahn, L. B. Skinner, and Y. Wang, *Proc. Natl. Acad. Sci. USA* **114**, 10041 (2017).
- [10] S. Petitgirard, W. J. Malfait, B. Journaux, I. E. Collings, E. S. Jennings, I. Blanchard, I. Kantor, A. Kurnosov, M. Cotte, T. Dane *et al.*, *Phys. Rev. Lett.* **119**, 215701 (2017).
- [11] M. Grimsditch, *Phys. Rev. Lett.* **52**, 2379 (1984).
- [12] R. J. Hemley, H. K. Mao, P. M. Bell, and B. O. Mysen, *Phys. Rev. Lett.* **57**, 747 (1986).
- [13] D. Wakabayashi, N. Funamori, T. Sato, and T. Taniguchi, *Phys. Rev. B* **84**, 144103 (2011).
- [14] M. Guthrie, C. A. Tulk, C. J. Benmore, J. Xu, J. L. Yarger, D. D. Klug, J. S. Tse, H.-k. Mao, and R. J. Hemley, *Phys. Rev. Lett.* **93**, 115502 (2004).
- [15] Y. Kono, C. Kenney-Benson, D. Ikuta, Y. Shibazaki, Y. Wang, and G. Shen, *Proc. Natl. Acad. Sci. USA* **113**, 3436 (2016).
- [16] S. Petitgirard, G. Spiekermann, K. Glazyrin, J. Garrevoet, and M. Murakami, *Phys. Rev. B* **100**, 214104 (2019).
- [17] Q. Li, B. Liu, L. Wang, D. Li, R. Liu, B. Zou, T. Cui, and G. Zou, *J. Phys. Chem. Lett.* **1**, 309 (2010).
- [18] Y. Shu, Y. Kono, I. Ohira, Q. Li, R. Hrubiak, C. Park, C. Kenney-Benson, Y. Wang, and G. Shen, *J. Phys. Chem. Lett.* **11**, 374 (2020).
- [19] A. G. Papadopoulos, N. S. Tagiara, E. Stavrou, F. Li, G. Yang, and E. I. Kamitsos, *J. Phys. Chem. Lett.* **14**, 387 (2023).

- [20] S. K. Lee, Y.-H. Kim, P. Chow, Y. Xiao, C. Ji, and G. Shen, *Proc. Natl. Acad. Sci. USA* **115**, 5855 (2018).
- [21] C. J. Benmore, J. K. R. Weber, S. Sampath, J. Siewenie, J. Urquidi, and J. A. Tangeman, *J. Phys.: Condens. Matter* **15**, S2413 (2003).
- [22] M. Licheron, V. Montouillout, F. Millot, and D. R. Neuville, *J. Non-Cryst. Solids* **357**, 2796 (2011).
- [23] J. W. E. Drewitt, L. Hennem, A. Zeidler, S. Jahn, P. S. Salmon, D. R. Neuville, and H. E. Fischer, *Phys. Rev. Lett.* **109**, 235501 (2012).
- [24] J. W. E. Drewitt, S. Jahn, C. Sanloup, C. de Grouchy, G. Garbarino, and L. Hennem, *J. Phys.: Condens. Matter* **27**, 105103 (2015).
- [25] J. Akola, S. Kohara, K. Ohara, A. Fujiwara, Y. Watanabe, A. Masuno, T. Usuki, T. Kubo, A. Nakahira, K. Nitta *et al.*, *Proc. Natl. Acad. Sci. USA* **110**, 10129 (2013).
- [26] L. B. Skinner, A. C. Barnes, P. S. Salmon, H. E. Fischer, J. W. E. Drewitt, and V. Honkimäki, *Phys. Rev. B* **85**, 064201 (2012).
- [27] J. Yu, Y. Arai, T. Masaki, T. Ishikawa, S. Yoda, S. Kohara, H. Taniguchi, M. Itoh, and Y. Kuroiwa, *Chem. Mater.* **18**, 2169 (2006).
- [28] K. Yoshimoto, A. Masuno, M. Ueda, H. Inoue, H. Yamamoto, and T. Kawashima, *Sci. Rep.* **7**, 45600 (2017).
- [29] A. Masuno, H. Inoue, K. Yoshimoto, and Y. Watanabe, *Opt. Mater. Express* **4**, 710 (2014).
- [30] A. Masuno, *J. Phys. Soc. Jpn.* **91**, 091003 (2022).
- [31] Y.-M. Sung and S.-J. Kwon, *J. Mater. Sci. Lett.* **18**, 1267 (1999).
- [32] G. A. Rosales-Sosa, A. Masuno, Y. Higo, H. Inoue, Y. Yanaba, T. Mizoguchi, T. Umada, K. Okamura, K. Kato, and Y. Watanabe, *Sci. Rep.* **5**, 15233 (2015).
- [33] Y. Guo, J. Li, Y. Zhang, S. Feng, and H. Sun, *iScience* **24**, 102735 (2021).
- [34] G. A. Rosales-Sosa, A. Masuno, Y. Higo, and H. Inoue, *Sci. Rep.* **6**, 23620 (2016).
- [35] Y. Arai, K. Itoh, S. Kohara, and J. Yu, *J. Appl. Phys.* **103**, 094905 (2008).
- [36] A. Masuno and H. Inoue, *Appl. Phys. Express* **3**, 102601 (2010).
- [37] K. Watanabe, T. Nakamura, and T. Morita, *Astrophys. J.* **961**, 129 (2024).
- [38] See Supplemental Material at <http://link.aps.org/supplemental/10.1103/PhysRevB.110.054115>, which includes the details of the sample synthesis and the supplemental data (Figs. S1–S9 and Tables S1–S4).
- [39] Y. Higo, Y. Kono, T. Inoue, T. Irifune, and K.-i. Funakoshi, *J. Synchrotron. Rad.* **16**, 762 (2009).
- [40] Y. Higo, T. Irifune, and K.-i. Funakoshi, *Rev. Sci. Instrum.* **89**, 014501 (2018).
- [41] S. Gréaux, T. Irifune, Y. Higo, Y. Tange, T. Arimoto, Z. Liu, and A. Yamada, *Nature (London)* **565**, 218 (2019).
- [42] T. Tsuchiya, *J. Geophys. Res.* **108**, 2462 (2003).
- [43] Y. Kono, C. Park, T. Sakamaki, C. Kenney-Benson, G. Shen, and Y. Wang, *Rev. Sci. Instrum.* **83**, 033905 (2012).
- [44] Y. Kono, C. Park, C. Kenney-Benson, G. Shen, and Y. Wang, *Phys. Earth Planet. Inter.* **228**, 269 (2014).
- [45] I. Ohira, Y. Kono, Y. Shibazaki, C. Kenney-Benson, A. Masuno, and G. Shen, *Geochem. Persp. Lett.* **10**, 41 (2019).
- [46] Y. Shu, Y. Kono, I. Ohira, R. Hrubciak, C. Kenney-Benson, M. Somayazulu, N. Velisavljevic, and G. Shen, *J. Phys. Chem. B* **124**, 7258 (2020).
- [47] Y. Kono, K. Ohara, N. M. Kondo, Y. Higo, S. Kakizawa, H. Yumoto, T. Koyama, H. Yamazaki, Y. Senba, H. Ohashi *et al.*, *Rev. Sci. Instrum.* **95**, 013904 (2024).
- [48] A. Pedone, G. Malavasi, M. C. Menziani, A. N. Cormack, and U. Segre, *J. Phys. Chem. B* **110**, 11780 (2006).
- [49] S. Jahn and P. A. Madden, *Phys. Earth Planet. Int.* **162**, 129 (2007).
- [50] J. W. E. Drewitt, S. Jahn, V. Cristiglio, A. Bytchkov, M. Leydier, S. Brassamin, H. E. Fischer, and L. Hennem, *Phys.: Condens. Matter* **23**, 155101 (2011); **24**, 099501 (2012).
- [51] H. Sakuma and K. Kawamura, *Geochim. Cosmochim. Acta* **73**, 4100 (2009).
- [52] L. Verlet, *Phys. Rev.* **159**, 98 (1967).
- [53] W. C. Swope, H. C. Andersen, P. H. Berens, and K. R. Wilson, *J. Chem. Phys.* **76**, 637 (1982).
- [54] J. W. E. Drewitt, *J. Phys.: Condens. Matter* **33**, 503004 (2021).
- [55] S. A. Amin, K. Leinenweber, C. J. Benmore, R. Weber, and J. L. Yarger, *J. Phys. Chem. C* **116**, 2068 (2012).
- [56] S. Li, J. J. Kweon, S. Lee, A. C. Lee, and S. K. Lee, *J. Phys. Chem. Lett.* **14**, 2078 (2023).
- [57] Q. Mei, C. J. Benmore, S. Sampath, J. K. R. Weber, K. Leinenweber, S. Amin, P. Johnston, and J. L. Yarger, *J. Phys. Chem. Solids* **67**, 2106 (2006); **68**, 315(E) (2007).
- [58] M. Wilson, P. A. Madden, N. N. Medvedev, A. Geiger, and A. Appelhagen, *J. Chem. Soc., Faraday Trans.* **94**, 1221 (1998).